

Experimental study of the solid-liquid interface in a yield-stress fluid flow upstream of a step

Li-Hua Luu* and Pierre Philippe

IRSTEA, UR OHAX, 3275 route de Cézanne, 13182 Aix-en-Provence, France

Guillaume Chambon

*IRSTEA, UR ETGR, Domaine Universitaire, BP 76, 38402 St-Martin-d'Hère, France
and Université Grenoble Alpes, 38402 St-Martin-d'Hère, France*

(Received 20 June 2014; revised manuscript received 14 October 2014; published 30 January 2015)

We present an experimental study investigating the transition zone between a liquid-like unyielded region and a solid-like yielded region in a yield-stress fluid. The configuration consists of a rectangular closed-channel flow disturbed by the presence of a step. Upstream of the step, a solid-liquid interface between a dead zone and a flow zone appears. In this study, we use a model fluid, namely polymer micro-gel Carbopol, which exhibits Herschel-Bulkley viscoplastic rheology. Exploiting the fluid transparency, the flow is monitored by particle image velocimetry using an internal visualization technique. The main outcome of this study is to show that, except in a thin transition layer close to the solid-liquid interface, the flow behaves as an apparent Poiseuille flow with an apparent slip condition at the base. The slip frontier is found to be almost independent of the flow rate while the corresponding slip velocity increases with the flow rate.

DOI: [10.1103/PhysRevE.91.013013](https://doi.org/10.1103/PhysRevE.91.013013)

PACS number(s): 47.57.—s, 83.80.Kn, 83.60.Fg, 83.60.La

I. INTRODUCTION

Yield-stress, or viscoplastic, fluids behave as solids below a certain stress threshold, namely the yield stress, and as viscous liquids above this threshold. Various familiar materials exhibit this type of flow threshold. A nonexhaustive list could include food and cosmetic creams, paints, blood, and slurries. These materials are involved in a variety of industrial [1], biophysical [2,3], and geophysical flows [4]. Even though the first mathematical description of the viscoplastic rheological behavior was formulated more than a century ago [5], some important issues remain open. In particular, the so-called solid-to-liquid transition, often compared to a jamming transition [6], is far from being fully understood [7–9].

In this paper, we intend to examine the close vicinity of the interface between a flowing liquid-like domain and an effective static solid-like domain in an homogeneous yield-stress fluid. This configuration is particularly relevant with regards to geophysical flows such as debris flows and snow avalanches [4], in which the material forming the static bed generally has mechanical properties similar to those of the flowing material. These rapid gravity-driven flows frequently induce massive bed erosion phenomena that remain poorly understood [10,11]. The knowledge of the frontier line between the substratum and the eroding flow is crucial to predicting mass exchanges with the bed and the flow dynamics [12,13]. The present experimental study proposes an original approach to address this process in terms of solid-fluid transition in a viscoplastic material.

The coexistence of solid and liquid behaviors in viscoplastic fluids, or in other words between yielded and unyielded regions, has been investigated in some recent studies on contraction-expansion flows [14–19], extrusion flows [20], and lid-driven cavity flows [21]. The shape and the extent of each region have been thoroughly investigated, but few

experimental studies have analyzed the detailed features of the velocity profile at the solid-liquid interface [19,20]. Chevalier *et al.* [19], in particular, introduced the notion of “frustrated” flow to describe the boundary layers created close to solid-liquid interfaces in such yield stress materials. The hydrodynamic configuration chosen in the present study consists of a steady flow in a rectangular channel in which an abrupt contraction is located. We focus on the specific velocity profiles above the dead zone appearing upstream of the contraction. Indeed, unlike Newtonian fluids for which sudden cross-section changes cause internal flow separations [22], viscoplastic fluids tends to smooth out the abrupt contraction by creating a dead zone, without flow recirculations upstream of the step, at least for sufficiently low Reynolds numbers and sufficiently high Herschel-Bulkley numbers [14,15].

The present paper is organized as follows. The experimental conditions and techniques, as well as the setup, are presented in Sec. II. Section III focuses on the flow far from the step where a classical Poiseuille flow configuration is recovered. Section IV presents a description of the flow above the dead zone, based on the detailed velocity profiles acquired. Section V demonstrates the persistence, above the dead zone, of a Poiseuille-like flow with an apparent slip boundary condition. Finally, a summary and a final discussion are proposed in Sec. VI.

II. EXPERIMENTAL SETUP**A. Model yield-stress fluid**

The fluid used in this experimental study is a solution of polymer microgel Carbopol at a 0.1 wt% concentration. In the literature, this material has been widely used as a model viscoplastic fluid in standard rheological measurements [23,24], channel configurations [16,25,26], drag-force studies [27,28], and more complex hydrodynamics such as gravity-driven free-surface flows [29–31], fingering instabilities [32,33], and drop impacts [34,35]. The choice for this yield-stress fluid is often related to its ease of preparation and to the stability

*li-hua.luu@irstea.fr

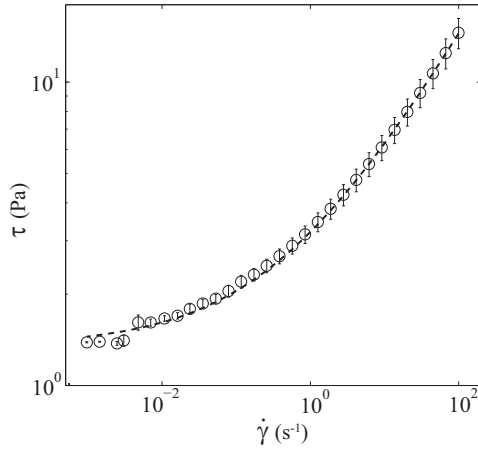


FIG. 1. Steady-state flow curves of the Carbopol solution used in this study: shear stress τ versus shear rate $\dot{\gamma}$ in log-log coordinates. The data points correspond to the average of two rheometrical tests. Error bars represent the variability between these tests. The dashed line corresponds to the best adjustment of the Herschel-Bulkley model given by Eq. (1) with $\tau_c = 1.36$ Pa, $K = 1.84$ Pa s n , and $n = 0.43$.

of its rheological properties over time (i.e., no significant thixotropy).

Carbopol solution rheology is thoroughly described by the Herschel-Bulkley (HB) model, which relates, in simple shear, shear stress τ to shear rate $\dot{\gamma}$ according to Refs. [36,37]:

$$\begin{aligned} \dot{\gamma} &= 0 & \text{for } \tau \leq \tau_c, \\ \tau &= \tau_c + K \dot{\gamma}^n & \text{for } \tau > \tau_c, \end{aligned} \quad (1)$$

where τ_c is the fluid yield stress, K is the fluid consistency, and n is the flow index. The preparation adopted in the present study follows a three-stage dispersing technique. First, 6 g of Carbopol powder (ETD 2623) are dissolved in 6 l of deionized water, under continuous and strong stirring at 1600 rpm for 3 h. Then the neutralization of the dispersion and the gelification require the addition of 14 ml of sodium

hydroxide at 0.5 mol l^{-1} . This volume has to be carefully injected at different regions of the solution using a pipette, avoiding any trapping of bubbles and stirring very slowly at 60 rpm, in order to ensure good homogenization. Finally, a post-mixing period under medium stirring at 800 rpm for 3 h gives a transparent gel.

Bulk rheological measurements of the fluid were carried out with a laboratory rheometer (Bohlin-CVOR), with a parallel plate geometry 60 mm in diameter. The tool surfaces have a roughness of around $400\text{--}500 \mu\text{m}$ in order to avoid wall slip [38,39]. Figure 1 shows the steady-state flow curve obtained with the Carbopol solution used in this study. Good agreement with the HB model is indeed observed, which provides the following rheological parameters: $\tau_c = 1.36$ Pa, $K = 1.84$ Pa s n , and $n = 0.43$. As detailed in Ref. [31], the typical errors associated with these rheometrical measurements result in uncertainties on the order of 10% for τ_c and K , and less than 2% for n . The density of the Carbopol solutions is considered to be the same as the density of water: $\rho = 1000 \text{ kg m}^{-3}$.

B. Setup and optical techniques

The experimental setup is illustrated in Fig. 2(a). This device consists of a closed-loop channel-flow facility, in which the flow rate is controlled by a gear pump (Verder VG 330.10, maximum flow rate of 288 l h^{-1}). To create a solid-liquid interface in the yield-stress fluid, a step 1.5 cm high is positioned inside the channel. Upstream of the step, the rectangular channel section is 6.9 cm high and 8 cm wide. To restrict slip, both the step and the bottom of the rectangular channel are made of mechanically abraded plexiglas surfaces characterized by a micron-size roughness. Top and lateral sides have been left smooth and transparent, to avoid disturbing the laser illumination and the flow visualization, but at the top wall it has been checked that slip nevertheless remains negligible, as discussed later. Roughening the plexiglas was therefore not necessary to prevent slip in these experiments.

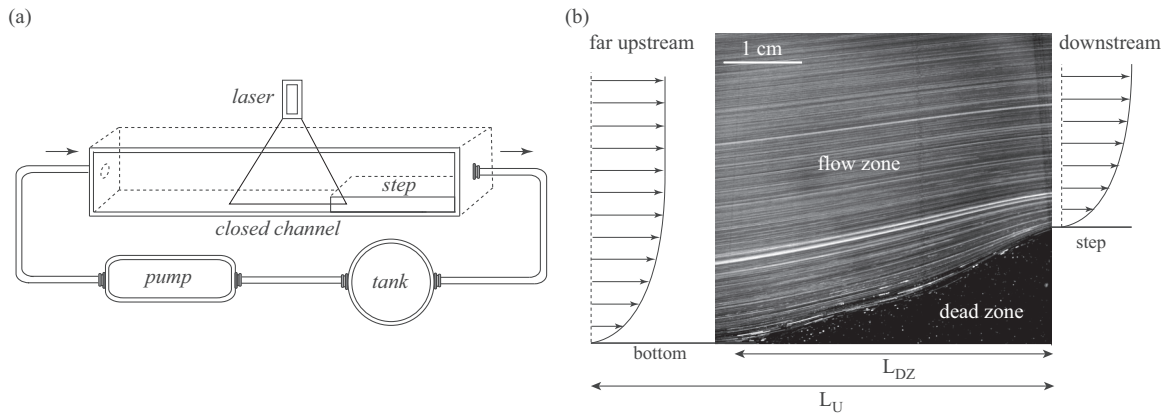


FIG. 2. (a) Schematic diagram of the experimental setup. The rectangular closed channel ($6.9 \times 8 \times 30 \text{ cm}^3$), which contains a step ($1.5 \times 8 \times 14 \text{ cm}^3$), is connected in input to a pump and in output to a tank, itself connected to the pump to form a closed loop. The laser system is fixed at half-width of the channel and illuminates the area upstream of the step. (b) Picture showing the flow of the yield-stress fluid at a flow rate $Q_p = 33.4 \text{ cm}^3 \text{ s}^{-1}$. Visualization of the streamlines and the dead zone results from the calculation of the pixel gray level standard deviation over 2723 images acquired at 50 Hz. The image resolution is 250 pix cm^{-1} . The classical Poiseuille velocity profiles recovered far upstream and downstream of the step are illustrated. The dead-zone basal extent is denoted L_{DZ} and the distance from the step, upstream of which the flow is uniform, is denoted L_U .

The principle of the experiment is to study the flow upstream of the step, by taking advantage of the transparent character of the Carbopol solutions that allows flow visualization. The solutions are seeded with micron-size glass hollow spheres (Aldrich, particle diameters, 9–13 μm ; density, 1100 kg m^{-3}), which are assumed to follow the streamlines as passive tracers and promote light reflection when the fluid is illuminated by a laser sheet. The position of the laser plane is set vertically at planar half-width of the channel. Pictures are taken using a monochrome digital camera at 50 Hz (Photron Fastcam SA3, 1024 \times 1024 pixels) with a macrolens (Sigma 180 mm F3.5 DG macro). To investigate the flow dynamics, we compute 2D velocity fields using a particle image velocimetry (PIV) algorithm. In this study, we are only interested in steady-state flows. Measurements are triggered at least 15 min after starting the pump, to ensure that the steady-state regime is fully developed. Velocity fields are averaged over a 1-min sequence in steady state. The PIV post-processing is performed by the free software DPIVsoft running in MATLAB [40].

Figure 2(b) displays the standard deviation of pixel gray levels over a 1-min sequence for a typical experiment. In this image, we can observe the streamlines and distinguish the interface between a yielded flow zone and an unyielded, and truly static, dead zone upstream of the step. The position of this interface, measured as the points where velocity profiles depart from zero, will be denoted y_{int} in the following. Two characteristic lengths are also indicated in Fig. 2(b): L_{DZ} is the basal extent of the dead zone and L_U denotes the distance from the step upstream of which the flow is uniform. Downstream of the step, uniform flows are almost immediately recovered. With the step height $D = 1.5$ cm, the order of magnitude of these lengths is $L_{\text{DZ}} \sim 3D$ and $L_U \sim 5.5D$ for all the pump flow rates studied. It should be noted that these typical lengths tend to slightly decrease when the flow rate increases, which indicates a progressive erosion of the dead zone. Along the channel, we can therefore distinguish two zones of uniform flow (far upstream of the step, at a distance greater than L_U , and downstream of the step) and a domain in between, where the flow is nonuniform due to the presence of the dead zone.

Table I gives a summary of the different experiments conducted for this study. From the rheological HB parameters τ_c , K , n , the pump flow rate Q_p , the channel width W and the flow height H ($H = 6.9$ cm upstream of the step and $H = 5.4$ cm downstream), we can compute the Herschel-Bulkley

TABLE I. Summary of the experiments carried out in this study: Q_p is the volumetric flow rate imposed by the pump, U is the mean velocity calculated by numerical integration of the experimental velocity profiles, Hb is the Herschel-Bulkley number, and Re is the generalized Reynolds number, calculated upstream and downstream of the step.

Q_p ($\text{cm}^3 \text{ s}^{-1}$)	U up. (cm s^{-1})	U down. (cm s^{-1})	Hb up.	Hb down.	Re up.	Re down.
14.8	0.17	0.22	2.70	2.15	0.006	0.008
33.4	0.59	0.74	1.57	1.29	0.040	0.052
52.0	1.01	1.25	1.25	1.03	0.094	0.118

number Hb and the generalized Reynolds number Re. The Hb number is defined as the ratio of the yield stress τ_c to a nominal shear stress $K(\frac{U}{H/2})^n$, where U is the mean velocity obtained by integrating the experimental velocity profile along the vertical direction y . Note that, due to 3D effects (see Appendix), the above characteristic velocity is slightly different from the $Q_p/(HW)$ value that would be derived directly from the pump flow rate. The Re number generalized to HB rheology is defined as the ratio of the hydrodynamic pressure ρU^2 to the nominal shear stress.

In this study, the Hb and Re numbers investigated range from 1 to 2.7, and from 0.006 to 0.118, respectively. According to previous numerical studies on similar flows [14,15], the values are too low to generate any recirculation flow in the corner upstream of the step, which is consistent with our observations [Fig. 2(b)].

III. POISEUILLE FLOW OF A HERSHEY-BULKLEY FLUID

We first examine the flow in the domains undisturbed by the step, i.e., far upstream and downstream of the step, to validate the relevance of the fluid's rheological description.

Without the influence of the step, the flow of the viscoplastic fluid is purely longitudinal. The velocity profile, $u = u(y)$, is almost symmetric with respect to the half-height of the channel. Figure 3 represents all the velocity half-profiles, for $0 \leq y \leq H/2$, upstream ($H = 6.9$ cm) and downstream ($H = 5.4$ cm) of the step. Velocity u is equal to zero at the boundaries (where the shear stress is maximum) and reaches a constant value in the central zone where the shear stress falls below the fluid yield stress, resulting in a plug flow in this central domain of the channel. Note that similar no-slip boundary conditions are recovered at the bottom and top walls, respectively, with and without surface roughening. Accordingly, no-slip boundary conditions are expected to hold at the lateral smooth walls. However, we show in the Appendix that the velocity profiles remain invariant in a large enough portion of the channel width to assume that velocity measurements at the center are unaffected by side effects.

We therefore assume that, far enough from the lateral walls, the flow can be described using the classical 2D Poiseuille equation:

$$0 = -\partial_x p + \partial_y \tau(y), \quad (2)$$

where the shear stress τ is given by the HB law [Eq. (1)], $\dot{\gamma} = \partial u / \partial y$. To solve this equation, we consider the pressure gradient $\partial_x p$ as constant, a condition imposed by symmetry in a longitudinal flow. However, we found, as expected, different values of this gradient far upstream and downstream of the step, due to the channel height change and the subsequent section reduction. It is important to note that, according to Eqs. (1) and (2), a constant pressure gradient is equivalent to a linear evolution of $\dot{\gamma}^n$ with y . Equation (2) can then be integrated with the following boundary conditions: $\partial_y u(y_{\text{plug}}) = 0$ and $u(0) = 0$, where y_{plug} denotes the position of the plug onset and $y = 0$ is the channel (upstream) or the step (downstream) bottom boundary.

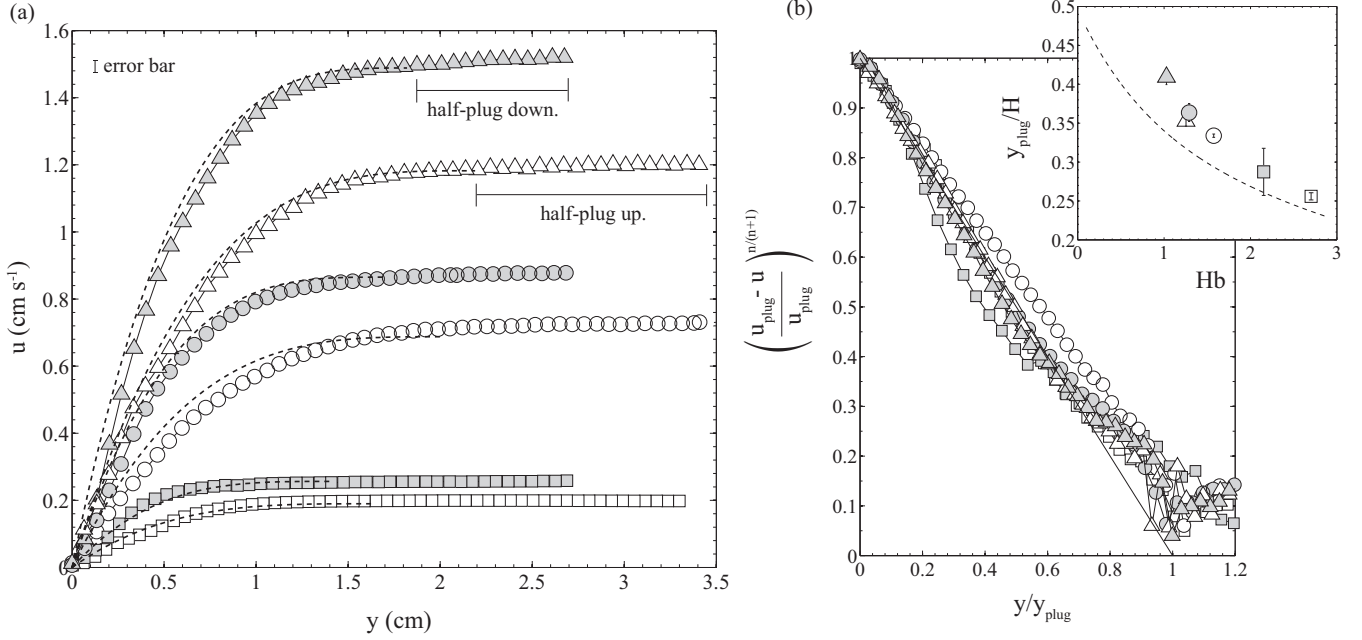


FIG. 3. (a) Velocity half-profiles far upstream (open symbols) and downstream (solid symbols) of the step for the three imposed flow rates $Q_p = 14.8 \text{ cm}^3 \text{ s}^{-1}$ (squares), $Q_p = 33.4 \text{ cm}^3 \text{ s}^{-1}$ (circles), $Q_p = 52.0 \text{ cm}^3 \text{ s}^{-1}$ (triangles). Dashed lines represent the theoretical predictions with no adjustable parameter (see text for greater detail). The error bar corresponds to an uncertainty of ± 1 pixel in the length calibration. (b) Dimensionless velocity half-profiles to the power $n/(n+1)$ as a function of dimensionless positions. The line indicates the theoretical relationship given by Eq. (4). Inset: dimensionless plug positions obtained by linear adjustments of Eq. (4), as a function of the Herschel-Bulkley number. The dashed line corresponds to the numerical solution of Eq. (5). Uncertainties represent the 95% confidence bounds of the fits.

The analytical expression for this Poiseuille flow of a Herschel-Bulkley fluid (PHB) can be written as

$$u = \begin{cases} \frac{n}{n+1} \left(-\frac{1}{K} \partial_x p\right)^{\frac{1}{n}} \left[y_{\text{plug}}^{\frac{n+1}{n}} - (y_{\text{plug}} - y)^{\frac{n+1}{n}} \right], & \text{for } 0 \leq y \leq y_{\text{plug}}, \\ \frac{n}{n+1} \left(-\frac{1}{K} \partial_x p\right)^{\frac{1}{n}} y_{\text{plug}}^{\frac{n+1}{n}} = u_{\text{plug}}, & \text{for } y_{\text{plug}} \leq y \leq \frac{H}{2}. \end{cases} \quad (3)$$

Outside of the plug zone, Eq. (3) can be rewritten as

$$\left(\frac{u_{\text{plug}} - u}{u_{\text{plug}}} \right)^{\frac{n}{n+1}} = 1 - \frac{y}{y_{\text{plug}}}. \quad (4)$$

The plug velocity u_{plug} is acquired from the experimental data [Fig. 3(a)] by averaging velocity values over the plateau-like domain. Given the rheological parameter $n = 0.43$, we can then use Eq. (4) to determine the onset position of the plug y_{plug} through a linear fit. Figure 3(b) shows a satisfactory agreement with the theoretical linear prediction, confirming the overall validity of the Poiseuille flow description.

To validate the values of y_{plug} inferred from the previous approach, we compared them to the independent theoretical predictions derived from the values of the fluid rheological parameters. Since the pressure gradient is constant, and acknowledging that the shear stress drops to zero at the center of the channel by symmetry, we can write $-\partial_x p = \tau_c / (\frac{H}{2} - y_{\text{plug}})$. Hence, by integrating the velocity profile given in Eq. (3), we obtain the following theoretical relationship

between y_{plug} and the Herschel-Bulkley number Hb :

$$1 = \frac{n}{n+1} \left(\frac{Hb}{1 - \frac{2y_{\text{plug}}}{H}} \right)^{\frac{1}{n}} \left(\frac{2y_{\text{plug}}}{H} \right)^{\frac{n+1}{n}} \left(1 - \frac{n}{2n+1} \frac{2y_{\text{plug}}}{H} \right). \quad (5)$$

The comparison between the two estimates of y_{plug} is represented in the inset of Fig. 3(b). We observe that the y_{plug}/H ratio directly deduced from the velocity profiles follows the general trend predicted by Eq. (5), but that the data are systematically slightly above the theoretical line. As suggested in a recent study [31], this discrepancy probably arises from the uncertainty on Carbopol rheological properties τ_c and K .

We compare the experimental velocity profiles to the theoretical predictions obtained with the value of y_{plug} deduced through Eq. (5). Indeed, recalling that $-\partial_x p = \tau_c / (\frac{H}{2} - y_{\text{plug}})$, the expression of velocity in Eq. (3) is now completely explicit. As shown in Fig. 3(a), we find rather good agreement between the experimental and theoretical profiles, given once again the uncertainty on Carbopol rheological properties [36,37]. To conclude, the various analyses presented in this section confirm that the channel flow far upstream and downstream of the step is consistent with a 2D Poiseuille flow description coupled to HB rheology. In particular, it appears that the velocities measured in the center of channel can indeed be regarded as unaffected by 3D side effects.

IV. FLOW ABOVE THE DEAD ZONE

In this section, we describe the velocity profiles measured in the vicinity of the step, above the solid-liquid interface.

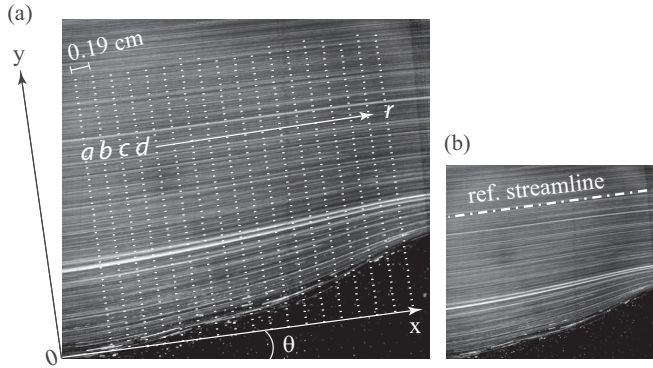


FIG. 4. (a) Reference frame (x, y) tilted by an angle θ from the horizontal, with an x axis parallel to the reference streamline indicated in (b). The velocity profiles are acquired along the dotted straight lines (from a to r).

A. Reference frame

Unlike for the longitudinal flow considered in the previous section, the presence of the step deviates the streamlines from the horizontal direction towards the center of the channel [Fig. 2(b)]. Nevertheless, we note that these streamlines remain almost parallel, at least far enough from the step corner and far enough above the dead zone. For greater insight into the flow behavior in this region, we chose to project the velocity profiles in a reference frame tilted by an angle θ which corresponds to the direction of the parallel streamlines (Fig. 4). Note that we keep the notation (x, y) for the sake of simplicity. The origin of the axes is fixed at the left edge of the dead zone and at the channel bottom boundary [Fig. 4(a)]. Figure 5 shows the longitudinal and transverse velocities u and v , projected in this tilted reference frame, for an imposed flow rate of $Q_p = 33.4 \text{ cm}^3 \text{ s}^{-1}$. The different profiles correspond to successive longitudinal positions a to r , indicated in Fig. 4. We observe that v exhibits maxima that do not exceed 0.06 cm s^{-1} for mean velocities varying between 0.6 cm s^{-1} and 0.7 cm s^{-1} . It therefore appears acceptable to consider v as second-order compared to u . In the following, we consequently assume, as a first approximation, that the flow in the tilted reference frame is purely longitudinal, and we focus on the analysis of the u velocity profiles along the x axis.

Looking at Fig. 5, it clearly appears that the position y_{int} where the velocity u departs from zero increases as we get closer to the step. The solid-liquid interface y_{int} defined from the velocity profiles matches the dead-zone border observed on the time-averaged picture (Fig. 5, inset). Far enough from the lateral walls, we check that this solid-liquid interface is invariant with respect to the transverse direction (see Appendix).

Far from the bottom boundary, a constant velocity plateau can be observed, indicating the presence of a plug, whose value increases when approaching the step. As will be explained in the next section, this velocity increase is related to the progressively diminishing flow section due to the presence of the dead zone.

In between the solid-liquid interface y_{int} and the plug-zone onset, a particular point of coordinates (y_s, u_s) can be observed,

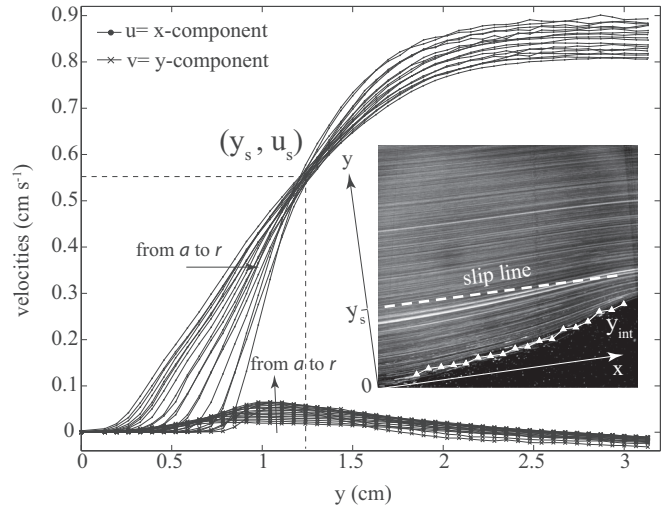


FIG. 5. Longitudinal and transverse velocity components u and v in the tilted reference frame for a flow rate $Q_p = 33.4 \text{ cm}^3 \text{ s}^{-1}$. The velocity profiles are acquired along the horizontal positions a to r . The particular point at which all u profiles intersect lies at the position $y_s = 1.42 \pm 0.03 \text{ cm}$ and corresponds to a velocity $u_s = 0.56 \pm 0.02 \text{ cm s}^{-1}$. Inset: image showing the slip line (dashed) $y = y_s$ and the solid-liquid interface $y = y_{int}$ acquired from the velocity profiles (symbols).

at which all u profiles intersect. This notable feature indicates that, in the tilted reference frame, there exists a line $y = y_s$ along which all velocity profiles have a constant value: $u(y_s) = u_s$ (Fig. 5, inset). This line will be called slip line in the following.

B. Different flow layers

Unlike for the Poiseuille flow, the velocity profiles shown in Fig. 5 exhibit a change in curvature. To highlight this inflexion point, Fig. 6 shows the shear-rate profiles, computed

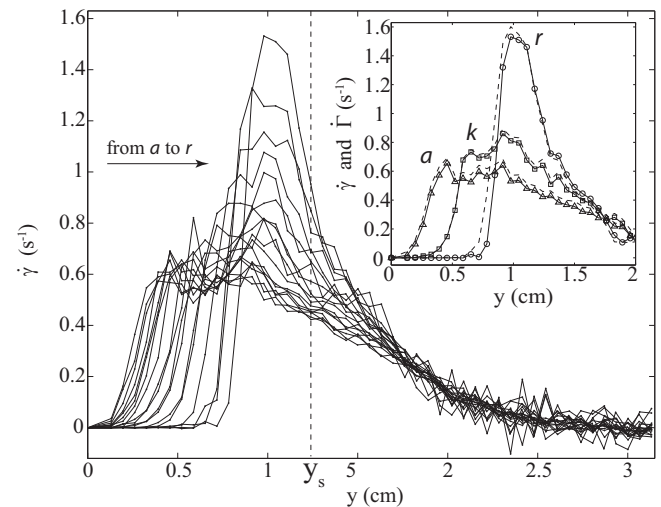


FIG. 6. Profiles of approximated shear rate $\dot{\gamma}$, calculated by numerical differentiation of u with respect to y , for the positions a to r (see Fig. 4). Inset: comparison between $\dot{\gamma}$ (symbols) and the complete shear rate $\dot{\Gamma}$ (dashed lines), for profiles a , k , and r .

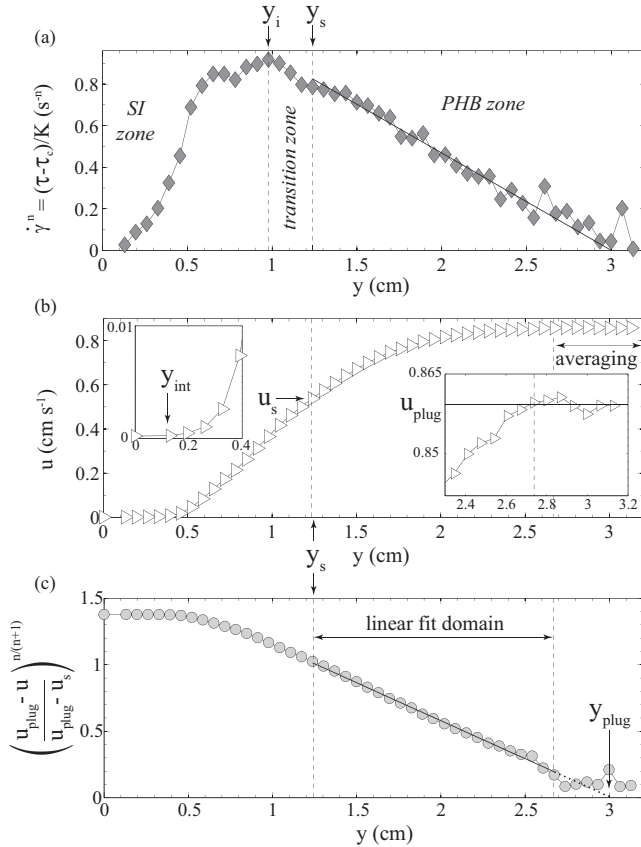


FIG. 7. At position k (see Fig. 4) for a pump-flow rate $Q_p = 33.4 \text{ cm}^3 \text{ s}^{-1}$: (a) profile of $\dot{\gamma}^n = (\tau - \tau_c)/K$ (the line gives a guide for the eye), (b) corresponding velocity profile u , with two close-ups at the dead zone and plug borders, and (c) ratio $(u_{\text{plug}} - u)/(u_{\text{plug}} - u_s)^{n/(n+1)}$ to the power $n/(n+1)$. More details on the different parameters indicated are provided in the text.

as $\partial u/\partial y$, for the different positions along the x axis. Before going further, let us discuss this approximation of the shear rate. In the inset of Fig. 6, we compare the approximated

value $\dot{\gamma} = \partial_y u$, to the complete shear rate defined as, in 2D, $\dot{\Gamma} = \sqrt{4(\partial_x u)^2 + (\partial_y u + \partial_x v)^2}$. Only minute differences are observed between the two quantities, and hence only $\dot{\gamma}$ will be considered in the following. This result implies that $|\partial_x u| \ll |\partial_y u|$, which is consistent with our assumption of a quasiparallel flow in the tilted reference frame.

All shear-rate profiles in Fig. 6 display an initial increase, starting at the solid-liquid interface, up to a maximal value corresponding to the velocity inflexion point and denoted by y_i in the following. The shear rate then presents a fluctuating plateau before decreasing toward the plug zone, where it reaches zero. The $\dot{\gamma}$ maxima, which are systematically located below the slip point y_s , show values that increase from positions a to r . Advancing toward the step, the growth-phase slope also gets slightly steeper and the plateau-like transition zone narrows. This gradual disappearance of the $\dot{\gamma}$ increasing and fluctuating phases, which leads to a purely decreasing phase, is consistent with the recovery of a pure Poiseuille-like behavior after the step.

Figure 7(a) shows profiles of $\dot{\gamma}^n$ (with $n = 0.43$), which, according to the HB constitutive law [Eq. (1)], is a quantity proportional to the shear stress τ . As expected, the shear stress is minimal, equal to τ_c , at the solid-liquid interface and in the central plug zone. Accordingly, the shear stress grows from the dead-zone border before decreasing to reach the central-plug zone, with a maximum at y_i . On one side, we call the region lying between y_{int} and y_i , the stress-increase (SI) zone. On the other side, beyond the slip position y_s , we observe that $\dot{\gamma}^n$ decreases linearly toward the plug zone. This behavior is reminiscent of the Poiseuille law [Eq. (2)], which predicts a constant derivative $d\tau/dy$. Consequently, the flow layer between y_s and the plug onset position y_{plug} will be named the PHB zone. The next section will be devoted to properly demonstrating that the flow in this zone can indeed be described with the PHB theory, including an apparent basal slip. Last, the narrow layer lying between the inflexion point y_s and the slip point y_s , is called the transition zone.

Figure 8(a) shows a visualization of these different flow layers for $Q_p = 33.4 \text{ cm}^3 \text{ s}^{-1}$. It can be noted that the

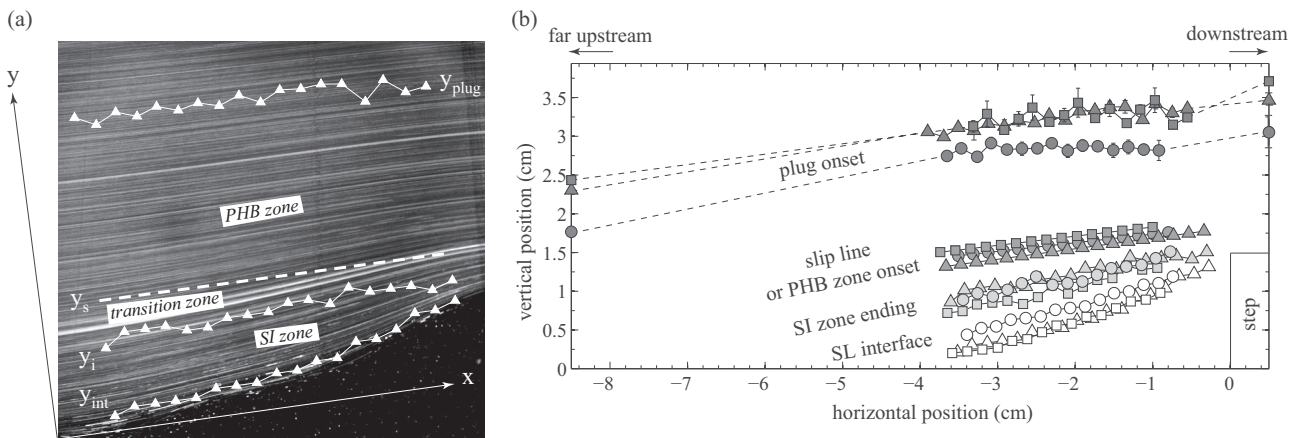


FIG. 8. (a) Delineation of the different flow layers: SI zone between y_{int} and y_i , transition zone between y_i and y_s , and PHB zone between y_s and y_{plug} , for $Q_p = 33.4 \text{ cm}^3 \text{ s}^{-1}$. (b) Map of the different flow-layer borders, for the three flow rates: $Q_p = 14.8 \text{ cm}^3 \text{ s}^{-1}$ (circles), $Q_p = 33.4 \text{ cm}^3 \text{ s}^{-1}$ (triangles), and $Q_p = 52.0 \text{ cm}^3 \text{ s}^{-1}$ (squares). Positions of the plug onset far upstream and downstream of the step are also displayed. The error bars on the solid-liquid interface position, the SI zone ending, and the slip-line determination, are smaller than symbol sizes. The uncertainties on plug onset position come from the 95% confidence bounds on linear fits (see Fig. 7).

solid-liquid interface is far from parallel to the x axis. This implies our assumption of a uniform flow in the tilted reference frame only applied far above the dead zone, typically beyond the transition zone. Figure 8(b) represents the SI and PHB zone borders for the three flow-rate values used in this study. Several interesting features emerge. First, it is observed that the slip lines almost coincide regardless of the flow rate. Similarly, leaving aside dispersion of the data, the SI zone ending positions also seem to be nearly superimposed. As a result, the transition zone is found to have the same width for the three flow-rate values. We also note a superposition of dead-zone borders and plug onset positions for the two highest flow rates, which possibly suggests a saturation phenomenon above a certain flow rate. On the contrary, the zone is wider for the lowest flow rate, the corresponding SI zone is smaller, and the plug onset position is lower.

V. SLIP LINE

The objective of this section is to demonstrate that, in the region located above the slip line, flow can be described by the PHB theory (presented in Sec. III) taking into account an apparent basal slip.

A. Poiseuille flow with a slip condition

Accounting for the existence of an apparent slip velocity u_s at the effective boundary condition $y = y_s$, Eq. (4) becomes (for $y_s < y < y_{\text{plug}}$)

$$\left(\frac{u_{\text{plug}} - u}{u_{\text{plug}} - u_s} \right)^{\frac{n}{n+1}} = 1 - \frac{y - y_s}{y_{\text{plug}} - y_s}. \quad (6)$$

Figure 7(b) displays a typical velocity profile where the slip point (y_s, u_s) is indicated. Following the approach presented in Sec. III, the plug velocity u_{plug} can be obtained by averaging velocity values over the plateau-like domain. Knowing the quantities u_s and y_s , and given the rheological parameter $n = 0.43$, we then obtain the onset position y_{plug} through a linear fit using Eq. (6) [Fig. 7(c)]. Figure 9 shows the values of $(u_{\text{plug}} - u)/(u_{\text{plug}} - u_s)$ as a function of $(y - y_s)/(y_{\text{plug}} - y_s)$ obtained for all the velocity profiles and the three flow rates investigated. In the PHB zone, for $y > y_s$, a clear collapse of all the data into a single trend is observed. The master curve follows the linear trend predicted by Eq. (6) (thick dashed line) almost perfectly. This good agreement reflects the relevance of using PHB theory with a slip condition to describe this upper part of the flow above the dead zone.

B. Evolution of the plug velocity

Figure 8(b) shows that the plug onset position measured in the PHB zone above the solid-liquid interface seems to connect smoothly with the plug positions obtained far upstream and downstream of the step. Moreover, as already noted from Fig. 5, plug velocity u_{plug} regularly and almost linearly increases while advancing toward the step, here again smoothly connecting the plug velocity values obtained far upstream and downstream of the step. To rationalize this behavior, we propose an approach based on the 2D mass balance along the channel. Disregarding possible 3D effects

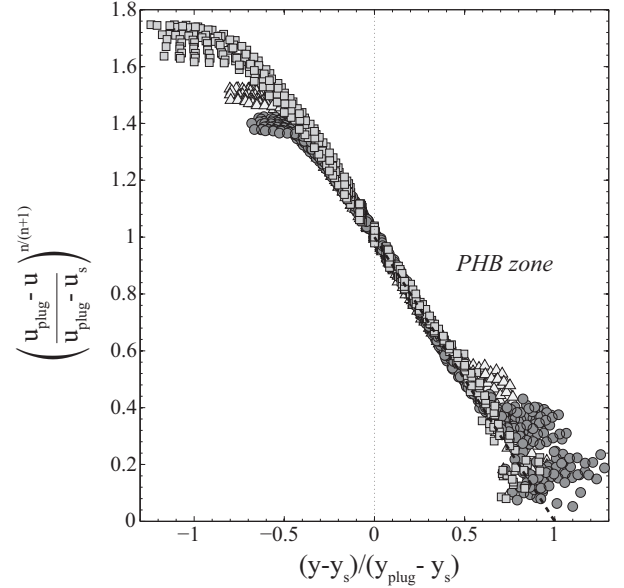


FIG. 9. Scaling obtained by plotting dimensionless velocities $(u_{\text{plug}} - u)/(u_{\text{plug}} - u_s)$ to the power $n/(n + 1)$ as a function of dimensionless positions $(y - y_s)/(y_{\text{plug}} - y_s)$, for different pump flow rates: $Q_p = 14.8 \text{ cm}^3 \text{ s}^{-1}$ (squares), $Q_p = 33.4 \text{ cm}^3 \text{ s}^{-1}$ (circles), and $Q_p = 52.0 \text{ cm}^3 \text{ s}^{-1}$ (triangles). The thick dashed line represents the theoretical prediction of Eq. (6).

(see Appendix), the flow rate Q_p can be written as

$$Q_p = W \int_0^H u(y) dy, \quad (7)$$

where u is defined in Eq. (4), W is the channel width, and H is the flow height. For a uniform Poiseuille flow (far upstream and downstream of the step), we obtain the following relation between plug velocity u_{plug} and flow rate Q_p :

$$u_{\text{plug}} = \frac{Q_p}{WH \left(1 - \frac{2n}{2n+1} \frac{y_{\text{plug}}}{H} \right)}. \quad (8)$$

Hence, whereas for a Newtonian fluid the maximum velocity would simply be half the mean velocity, in the present case, the relationship between the maximum velocity, i.e., u_{plug} , and the mean velocity defined by Q_p/WH depends on the rheological parameter n and the y_{plug}/H ratio.

To extend the above relation to the solid-liquid interface domain, we suggest simplifying the velocity profile by considering the portion below the slip position y_s as approximately linear, as illustrated in Fig. 10(a). Three typical lengths can then be defined: $H' = H - y_{\text{int}}$, $\delta_{\text{plug}} = y_{\text{plug}} - y_s$, and $\delta_s = y_s - y_{\text{int}}$. The velocity profile can be integrated by assuming, moreover, that the flow rate in the bottom half of the flow region, namely $0 < y - y_{\text{int}} < H'/2$, is exactly half of the total flow rate Q_p . The resulting flow rate is composed of a Poiseuille-type part for $u > u_s$ and a part for $u < u_s$, which reads $u_s W (H'/2 - \delta_s) + u_s W \delta_s / 2 = u_s W (H' - \delta_s) / 2$. By introducing the flow rate $Q_{\text{eff}} = Q_p - u_s W (H' - \delta_s)$, we can finally write the following generalized relationship for

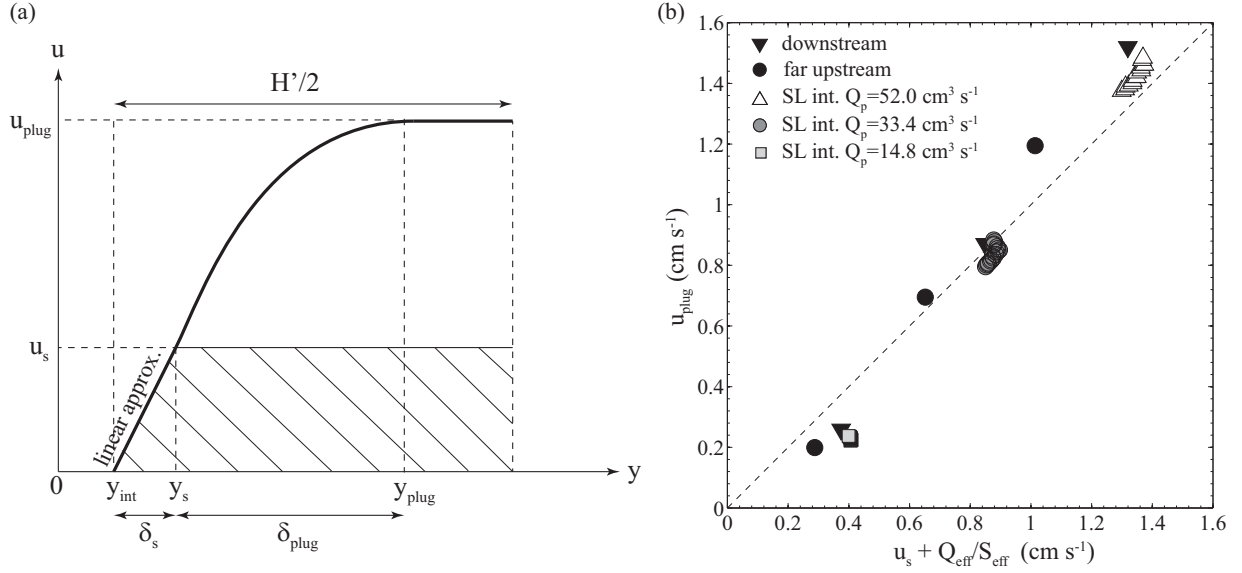


FIG. 10. (a) Schematic representation of a typical velocity half-profile in the domain above the dead zone. Greater detail is provided in the text. (b) Plug velocity u_{plug} measured for the three flow rates, far upstream and downstream of the step, and above the dead zone, as a function of the modified average velocity $u_s + Q_{\text{eff}}/S_{\text{eff}}$, where the effective flow rate Q_{eff} and section S_{eff} are defined in the text. The dashed line represents the bisector. Error bars on u_{plug} are smaller than symbol sizes and come from standard deviations on the direct measurements of the velocity values inside the plug zone.

u_{plug} , which takes into account the apparent slip u_s :

$$u_{\text{plug}} = u_s + \frac{Q_{\text{eff}}}{W(H' - 2\delta_s)\left(1 - \frac{2n}{2n+1} \frac{\delta_{\text{plug}}}{H' - 2\delta_s}\right)}. \quad (9)$$

Note that far upstream and downstream of the step, where $u_s = 0$ and $y_s = y_{\text{int}} = 0$, Eq. (8) is obviously recovered. Figure 10(b) represents u_{plug} as a function of the quantity $u_s + Q_{\text{eff}}/S_{\text{eff}}$, where $S_{\text{eff}} = W(H' - 2\delta_s)\left(1 - \frac{2n}{2n+1} \frac{\delta_{\text{plug}}}{H' - 2\delta_s}\right)$, for all

the measured velocity profiles with the three flow rates studied. All the data are quite satisfactorily gathered onto the tendency predicted by Eq. (9). Focusing first on the far upstream and downstream of the step zones, the discrepancy between the experimental data and the 2D prediction of Eq. (8) is less than 30%. This quantitative discrepancy can be attributed to the 3D effects that are not accounted for in the previous flow rate estimates (see Appendix). Regarding the data obtained above the solid-liquid interface, good agreement with the

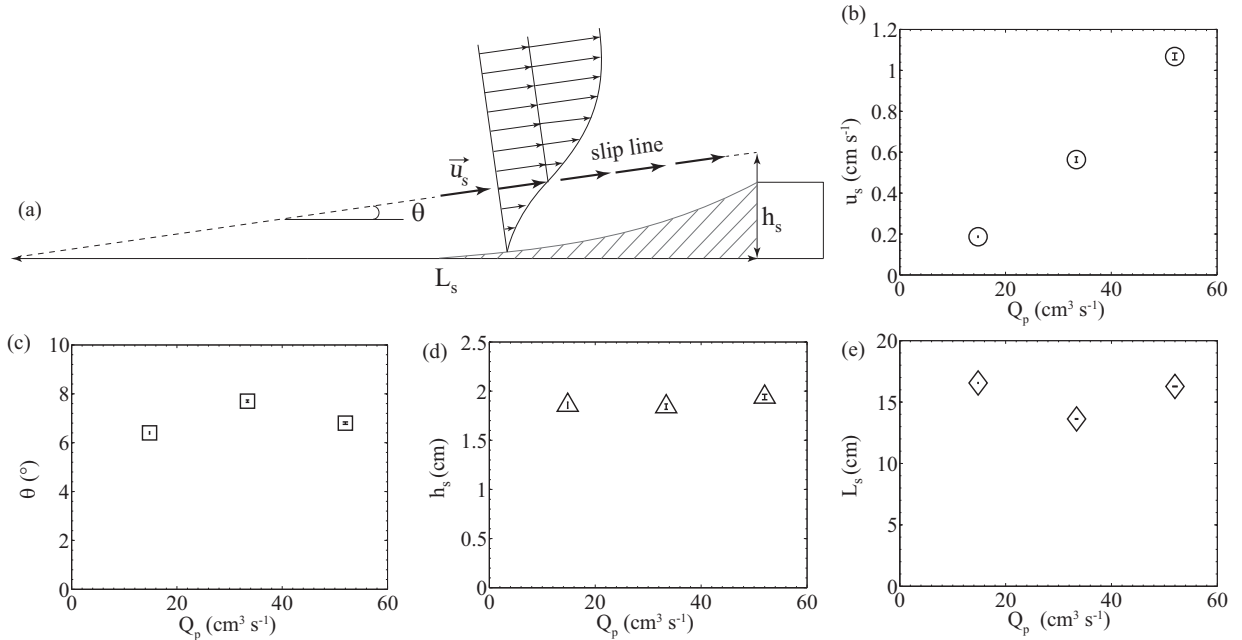


FIG. 11. (a) Illustration of the flow above the dead zone (shaded area). (a) Inclination angle θ of the x axis, (b) slip velocity u_s , (c) height h_s , and length L_s obtained by extrapolation of the slip line, as a function of flow rate Q_p .

theoretical prediction confirms that, except for a thin transition layer, the flow in this region can be described as a Poiseuille flow in a channel with varying cross sections, provided an apparent slip velocity is accounted for. Interestingly, this approach allows us to rationalize, within the same framework, the evolution of u_{plug} with Q_p for all of the flow along the channel.

C. Evolution of the slip line with flow parameters

Figure 11(a) shows the flow above the dead zone, including the slip line that marks the transition between the PHB flow zone above and the transition and SI zones below. We already mentioned (Sec. IV B) that the position of this slip line appears almost independent of the flow rate Q_p . Here, we characterize this line by different geometrical parameters, whose evolution with Q_p is studied in greater detail. As shown in Figs. 11(c)–11(e), none of these geometrical parameters, namely the inclination angle θ of the slip line, i.e., the inclination of the tilted reference frame, the height h_s extrapolated from the slip line at the edge of the step, and the horizontal length $L_s = h_s/\tan\theta$, appear to depend significantly on Q_p within the range studied. It should also be noted that despite the lack of measurements further upstream of the step, we expect that the slip line cannot remain straight at the approach of the bottom boundary where velocity is equal to zero. Once again, we emphasize that this notion of slip, and more generally the tilted reference frame validity, are only relevant in the scope of a local-scale study above the dead zone and far enough from the step.

VI. SUMMARY AND FINAL DISCUSSION

The present study was carried out to investigate the coexistence between solid-like and liquid-like regions in a yield-stress fluid flow. Experiments involving the flow of Carbopol solutions in a rectangular channel with a step were conducted. In the conditions of this study, with Hb numbers on the order of 1 and Re numbers varying between 0.01 and 0.1, a static domain forms upstream of the step, without any recirculation flow [14,15]. Using optical monitoring, we gained insight into the internal flow dynamics through PIV measurements. The main work in this paper concerned the detailed measurements of the velocity profiles above the dead zone. We demonstrated that Poiseuille hydrodynamics, including Herschel-Bulkley rheology (PHB), describe the flow from the plug almost to the solid-liquid interface, consistently with the flow far upstream and downstream of the step. However, the existence of an apparent slip line needs to be considered. Above this frontier, velocity profiles acquired in a tilted reference frame parallel to the streamlines increase from a constant value (assimilated to the slip velocity) and are well-adjusted by the PHB prediction. It was also found that flow rate only influences the value of the slip velocity but does not change the location of the slip line. Finally, we also qualitatively described the flow in between the slip line and the dead-zone border. Unlike the classical Poiseuille flow whose maximum shear rate occurs at the boundary, we observed that the shear rate at the static domain border was zero and increased up to a maximum in the vicinity of the slip

line. This specific stress-increase zone connects the boundary condition imposed by the dead zone ($\tau = \tau_c$ and $\dot{\gamma} = 0$) to the Poiseuille-like flow above.

One could wonder to what extent the slip line concept proposed in this paper could be generalized to other flow configurations involving the formation of a solid-liquid interface in yield-stress fluids. In Ref. [20] the authors report on velocity profiles in an extrusion flow and in particular in the vicinity of the die entrance, where a dead zone forms. Unfortunately, the spatial resolution of velocity measurements in this study appears too low to identify a potential slip line. More recently, another experimental study on frustrated viscoplastic flows [19] reports on velocity profiles that present similarities with those observed in the present study. In this paper, the velocity profiles in the boundary layer separating two unyielded regions is described as almost linear. Our experiments, with a higher spatial resolution, reveal more complex hydrodynamics in this boundary layer. We actually observe a zone where the shear rate is approximately constant but is not directly connected to the dead-zone border. In the vicinity of the solid-liquid interface, the plateau-like shear rate layer zone is preceded by a zone in which the shear rate rapidly increases, thus fulfilling the condition $\tau = \tau_c$ on the interface. On the other side, connection with the central plug zone where $\tau = \tau_c$ again occurs through a Poiseuille-like layer. Similar to Ref. [19], we found that the total size of this boundary layer (i.e., from y_{int} to y_{plug}) tends to decrease as the flow rate decreases [Fig. 8(b)].

Further understanding of the flow behavior above the dead zone will require a closer investigation of velocity profiles evolution between the solid-liquid interface and the slip line. In Fig. 9, it can already be noted that the collapse predicted by the PHB model is no longer achieved for $y < y_s$. This indicates that important ingredients are missing in this model to describe the full velocity profile in a single framework. In particular, the assumption of a purely longitudinal flow in the tilted reference frame, cannot be applied in the SI zone where the transverse velocity components become nonnegligible. More refined analyses will be necessary to focus specifically on this stress-increase zone.

ACKNOWLEDGMENTS

We thank Y. Forterre and his group GEP (IUSTI, Marseille) for allowing us to perform several preliminary tests on their rheometer and P. Freydier (IRSTEA, ETGR, Grenoble), who performed the rheometrical measurements presented in this paper. L.-H.L. acknowledges support through a Postdoctoral Grant funded by IRSTEA (France).

APPENDIX: 3D VELOCITY PROFILE

To evaluate the 3D effects involved in this experiment, we carried out a specific study to measure velocity fields outside of the channel midplane, for both the Poiseuille flow domains far upstream of the step and the flow above the dead zone. The laser was mounted on a translation stage, allowing us to scan the entire channel width. PIV measurements were acquired every 1 cm along the z axis. Note that the fluid used in these experiments has slightly different rheological parameters than

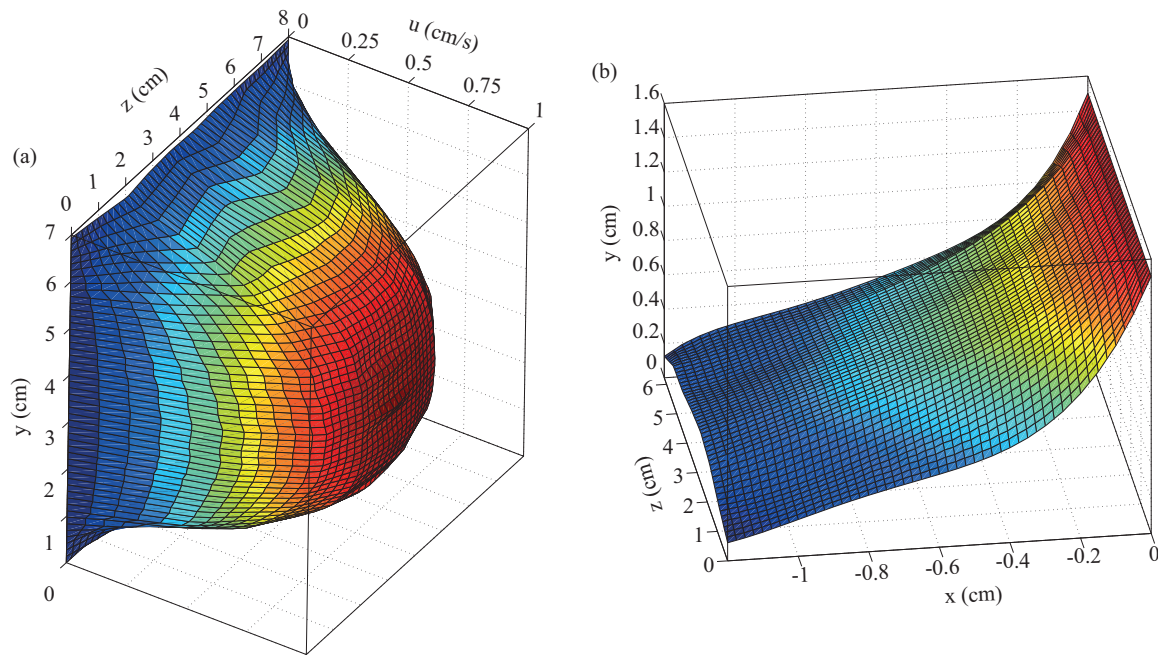


FIG. 12. (Color online) (a) 3D longitudinal velocity mapping in the uniform flow far upstream of the step, and (b) 3D mapping of the solid-liquid interface, for a Carbopol solution at 0.1 wt% whose HB parameters are: $\tau_c = 0.83$ Pa, $K = 1.42$ Pa sⁿ, and $n = 0.44$, for a flow rate $Q_p = 31.1$ cm³ s⁻¹.

for the rest of our results (Fig. 12). Figure 12(a) shows the 3D velocity map obtained by linear interpolation of the PIV data. We observe a well-defined central plug zone whose extension along the z axis occupies approximately 40% of the width. The 2D analysis performed in this paper is based on the existence of this large zone invariant with z in the center of the channel. Lateral boundaries therefore seem to induce similar shearing as the top and bottom boundaries.

We also investigated how the lateral boundaries and corners affect the shape of the solid-liquid interface [Fig. 10(b)]. We note that, in a first approximation, this interface can be considered to be independent of z except close to the lateral boundaries, where a slight excavation can be noted, probably due to the additional shearing undergone by the fluid in this zone. Thus, once again, a 2D description of the velocity profiles appears sufficient far enough from the lateral walls.

-
- [1] R. B. Bird, G. C. Dai, and B. J. Yarusso, The rheology and flow of viscoplastic materials, *Rev. Chem. Eng.* **1**, 1 (1983).
- [2] S. E. Charm and G. S. Kurland, Static method for determining blood yield stress, *Nature* **216**, 1121 (1967).
- [3] G. B. Thurston, Viscoelasticity of human blood, *Biophys. J.* **12**, 1205 (1972).
- [4] C. Ancey, Plasticity and geophysical flows: A review, *J. Non-Newtonian Fluid Mech.* **142**, 4 (2007).
- [5] E. Bingham, The behavior of plastic materials, *Bull. US Bureau Standards* **13**, 309 (1916).
- [6] E. Weeks, in *Statistical Physics of Complex Fluids*, edited by S. Maruyama and M. Tokuyama (Tohoku University Press, Sendai, Japan, 2007).
- [7] H. A. Barnes, The yield stress—a review or $\pi\alpha V T \alpha \rho \epsilon I$ —everything flows? *J. Non-Newtonian Fluid Mech.* **81**, 133 (1999).
- [8] F. Da Cruz, F. Chevoir, D. Bonn, and P. Coussot, Viscosity bifurcation in granular materials, foams, and emulsions, *Phys. Rev. E* **66**, 051305 (2002).
- [9] P. Coussot, N. Roussel, S. Jarny, and H. Chanson, Continuous or catastrophic solid-liquid transition in jammed systems, *Phys. Fluids* **17**, 011704 (2005).
- [10] M. Naaim, F. Naaim-Bouvet, T. Faug, and A. Bouchet, Dense snow avalanche modeling: flow, erosion, deposition and obstacle effects, *Cold. Reg. Sci. Technol.* **39**, 193 (2004).
- [11] S. McDougall and O. Hungr, Dynamic modelling of entrainment in rapid landslides, *Can. Geotech. J.* **42**, 1437 (2005).
- [12] R. M. Iverson, Elementary theory of bed-sediment entrainment by debris flows and avalanches, *J. Geophys. Res. Earth Surf.* **117**, F03006 (2012).
- [13] S. W. McCoy, J. W. Kean, J. A. Coe, G. E. Tucker, D. M. Staley, and T. A. Wasklewicz, Sediment entrainment by debris flows: In situ measurements from the headwaters of a steep catchment, *J. Geophys. Res. Earth Surf.* **117**, F03016 (2012).
- [14] P. Jay, A. Magnin, and J. M. Piau, Viscoplastic fluid flow through a sudden axisymmetric expansion, *AIChE J.* **47**, 2155 (2001).
- [15] A. N. Alexandrou, T. M. McGilvray, and G. Burgos, Steady Herschel–Bulkley fluid flow in three-dimensional expansions, *J. Non-Newtonian Fluid Mech.* **100**, 77 (2001).
- [16] P. R. de Souza Mendes, M. F. Naccache, P. R. Vargas, and F. H. Marchesini, Flow of viscoplastic liquids through axisymmetric expansions—contractions, *J. Non-Newtonian Fluid Mech.* **142**, 207 (2007).

- [17] B. Nassar, P. R. de Souza Mendes, and M. F. Naccache, Flow of elasto-viscoplastic liquids through an axisymmetric expansion–contraction, *J. Non-Newtonian Fluid Mech.* **166**, 386 (2011).
- [18] L. Hermany, D. D. O. dos Santos, S. Frey, M. F. Naccache, and P. R. de Souza Mendes, Flow of yield-stress liquids through an axisymmetric abrupt expansion-contraction, *J. Non-Newtonian Fluid Mech.* **201**, 1 (2013).
- [19] T. Chevalier, S. Rodts, X. Chateau, J. Boujlel, M. Maillard, and P. Coussot, Boundary layer (shear-band) in frustrated viscoplastic flows, *Europhys. Lett.* **102**, 48002 (2013).
- [20] B. D. Rabideau, P. Moucheront, F. Bertrand, S. Rodts, N. Roussel, C. Lanos, and P. Coussot, The extrusion of a model yield stress fluid imaged by MRI velocimetry, *J. Non-Newtonian Fluid Mech.* **165**, 394 (2010).
- [21] D. D. O. dos Santos, S. Frey, and M. F. Naccache, Numerical approximations for flow of viscoplastic fluids in a lid-driven cavity, *J. Non-Newtonian Fluid Mech.* **166**, 667 (2011).
- [22] B. F. Armaly, F. Durst, J. C. F. Pereira, and B. Schonung, Experimental and theoretical investigation of backward-facing step flow, *J. Fluid Mech.* **127**, 473 (1983).
- [23] A. Magnin and J. M. Piau, Cone-and-plate rheometry of yield stress fluids. Study of an aqueous gel, *J. Non-Newtonian Fluid Mech.* **36**, 85 (1990).
- [24] T. Divoux, D. Tamarii, C. Barentin, and S. Manneville, Transient shear banding in a simple yield stress fluid, *Phys. Rev. Lett.* **104**, 208301 (2010).
- [25] J. Peixinho, C. Nouar, C. Desaubry, and B. Théron, Laminar transitional and turbulent flow of yield stress fluid in a pipe, *J. Non-Newtonian Fluid Mech.* **128**, 172 (2005).
- [26] B. Guzel, T. Burghilea, I. A. Frigaard, and D. M. Martinez, Observation of laminar–turbulent transition of a yield stress fluid in Hagen–Poiseuille flow, *J. Fluid Mech.* **627**, 97 (2009).
- [27] D. D. Atapattu, R. P. Chhabra, and P. H. T. Uhlherr, Creeping sphere motion in Herschel-Bulkley fluids: Flow field and drag, *J. Non-Newtonian Fluid Mech.* **59**, 245 (1995).
- [28] H. Tabuteau, P. Coussot, and J. R. de Bruyn, Drag force on a sphere in steady motion through a yield-stress fluid, *J. Rheol.* **51**, 125 (2007).
- [29] G. Chambon, A. Ghemmour, and D. Laigle, Gravity-driven surges of a viscoplastic fluid: An experimental study, *J. Non-Newtonian Fluid Mech.* **158**, 54 (2009).
- [30] C. Ancey and S. Cochard, The dam-break problem for Herschel–Bulkley viscoplastic fluids down steep flumes, *J. Non-Newtonian Fluid Mech.* **158**, 18 (2009).
- [31] G. Chambon, A. Ghemmour, and M. Naaim, Experimental investigation of viscoplastic free-surface flows in a steady uniform regime, *J. Fluid Mech.* **754**, 332 (2014).
- [32] A. Lindner, P. Coussot, and D. Bonn, Viscous fingering in a yield stress fluid, *Phys. Rev. Lett.* **85**, 314 (2000).
- [33] K. E. Holloway, H. Tabuteau, and J. R. de Bruyn, Spreading and fingering in a yield-stress fluid during spin coating, *Rheol. Acta* **49**, 245 (2010).
- [34] L. H. Luu and Y. Forterre, Drop impact of yield-stress fluids, *J. Fluid Mech.* **632**, 301 (2009).
- [35] L. H. Luu and Y. Forterre, Giant drag reduction in complex fluid drops on rough hydrophobic surfaces, *Phys. Rev. Lett.* **110**, 184501 (2013).
- [36] F. K. Opong, L. Rubatat, B. J. Frisken, A. E. Bailey, and J. R. de Bruyn, Microrheology and structure of a yield-stress polymer gel, *Phys. Rev. E* **73**, 041405 (2006).
- [37] J. M. Piau, Carbopol gels: Elastoviscoplastic and slippery glasses made of individual swollen sponges: Meso- and macroscopic properties, constitutive equations and scaling laws, *J. Non-Newtonian Fluid Mech.* **66**, 051305 (2007).
- [38] A. Magnin and J. M. Piau, Cone-and-plate rheometry of yield stress fluids. Study of an aqueous gel, *J. Non-Newtonian Fluid Mech.* **23**, 91 (1987).
- [39] H. A. Barnes, A review of the slip (wall depletion) of polymer solutions, emulsions and particle suspensions in viscometers: Its cause, character, and cure, *J. Non-Newtonian Fluid Mech.* **56**, 221 (1995).
- [40] Open-source software developed by P. Meunier and T. Leweke at the IRPHE laboratory in Marseille, France.